Freeze-frame inhibitor captures acetylcholinesterase in a unique conformation

Yves Bourne*†, Hartmuth C. Kolb‡, Zoran Radić§, K. Barry Sharpless‡¶, Palmer Taylor§, and Pascale Marchot†‖

‖Ingénierie des Protéines, Centre National de la Recherche Scientifique Unité Mixte de Recherche–6560, Institut Fédératif de Recherche Jean Roche, Université de la Méditerranée, Faculté de Médecine Secteur Nord, F-13916 Marseille Cedex 20, France; *Architecture et Fonction des Macromolécules Biologiques, Centre National de la Recherche Scientifique Unité Mixte de Recherche–6098, 31 Chemin Joseph Aiguier, F-13402 Marseille Cedex 20, France; ‡Department of Chemistry, ¶The Skaggs Institute for Chemical Biology, The Scripps Research Institute, La Jolla, CA 92037; and §Department of Pharmacology, University of California at San Diego, La Jolla, CA 92093-0636

Contributed by K. Barry Sharpless, December 10, 2003

The 1,3-dipolar cycloaddition reaction between unactivated azides and acetylenes proceeds exceedingly slowly at room temperature. However, considerable rate acceleration is observed when this reaction occurs inside the active center gorge of acetylcholinesterase (AChE) between certain azide and acetylene reactants, attached via methylene chains to specific inhibitor moieties selective for the active center and peripheral site of the enzyme. AChE catalyzes the formation of its own inhibitor in a highly selective fashion: only a single *syn1*-triazole regioisomer with defined substitution positions and linker distances is generated from a series of reagent combinations. Inhibition measurements revealed this *syn1*-triazole isomer to be the highest affinity reversible organic inhibitor of AChE with association rate constants near the diffusion limit. The corresponding *anti1* isomer, not formed by the enzyme, proved to be a respectable but weaker inhibitor. The crystal structures of the *syn1*- and *anti1*-mouse AChE complexes at 2.45- to 2.65-Å resolution reveal not only substantial binding contributions from the triazole moieties, but also that binding of the *syn1* isomer induces large and unprecedented enzyme conformational changes not observed in the *anti1* complex nor predicted from structures of the apoenzyme and complexes with the precursor reactants. Hence, the freeze-frame reaction offers both a strategically original approach for drug discovery and a means for kinetically controlled capture, as a high-affinity complex between the enzyme and its self-created inhibitor, of a highly reactive minor abundance conformer of a fluctuating protein template.

Acetylcholinesterase (AChE) rapidly terminates cholinergic neurotransmission by catalyzing the hydrolysis of the neurotransmitter, acetylcholine, and inhibitors of AChE have been used for over a century in various therapeutic regimens (1, 2). The structure of the target enzyme reveals a narrow gorge ≈20 Å in depth with the catalytic triad of the active center at its base (3). Distinctive inhibitors bind to the active center or to a peripheral anionic site (PAS) located at the rim of the gorge near the enzyme surface (4–6). Previously, we generated a library of active site and PAS inhibitors with respective tacrine and phenanthridinium nuclei, each equipped with an azide or acetylene group at the end of a flexible methylene chain, to enable the reporting 1,3-dipolar cycloaddition to occur (Scheme 1) (7). AChE itself served as the reaction vessel, synthesizing its own inhibitor from these building blocks, in effect, by equilibrium-controlled sampling of various possible pairs of reactants in its active center gorge until irreversible cycloaddition between azide and acetylene ensued at an intersecting point within the gorge, between the two anchoring positions. From 49 building block combinations, the enzyme selected the TZ2/PA6 pair to form, with an enhanced reaction rate, a highly regioselective *syn1* triazole as the sole product (Scheme 1). In contrast, chemical synthesis by thermal reaction in the absence of enzyme proceeds very slowly and provides an ≈1:1 mixture of *syn1* and *anti1* regioisomers, which differ in the nitrogen substitution positions on the 1,2,3-triazole. Although both are high-affinity inhibitors, the *syn1* isomer, with a 100-fold greater affinity and a subpicomolar dissociation constant for certain AChEs (7), has a potency greater than all known noncovalent organic AChE inhibitors and high selectivity for individual cholinesterases.

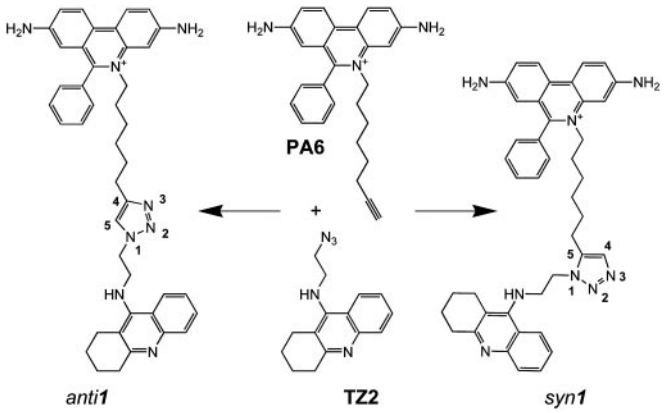

Scheme 1. Structures of the *anti1* and *syn1* TZ2PA6 regioisomers formed by 1,3-dipolar cycloaddition (7). The phenylphenanthridinium, triazole, and tacrine moieties are shown from top to bottom.

The discovery that enzymes can serve as atomic-scale reaction templates for creating their own inhibitors offers an original approach to drug discovery. In this light, we have solved the crystal structures of complexes of mouse AChE (mAChE) (8, 9) with the TZ2PA6 *anti1* and *syn1* regioisomers at 2.45- and 2.65-Å resolution (Table 1 and Fig. 1) and have analyzed further their respective binding kinetics and affinities (Table 2). We show that the distinctive binding properties of the two isomers in solution are related to discrete rearrangements in both the ligand and enzyme conformations. Indeed, the active center gorge and PAS conformations for the two crystalline complexes differ greatly, where binding of the higher affinity *syn1* isomer unveils a unique enzyme conformation not predicted from the structures of either the apo form or the complexes with the precursor reactants (10, 11). Hence these structures reveal that the *syn1* compound specifically formed on the enzyme effectively freezes in frame a highly reactive AChE conformer, and that the two TZ2PA6 regioisomers select distinct conformations from an unliganded enzyme that is presumably fluctuating between multiple conformational states. Because the unique structural features seen for the *syn1*–mAChE complex likely reflect the unique proximity

Abbreviations: AChE, acetylcholinesterase; mAChE, mouse AChE; PAS, peripheral anionic site.

Data deposition: The atomic coordinates and structure factors of the *anti1*- and *syn1*-mAChE complex structures have been deposited in the Protein Data Bank, www.rcsb.org (PDB ID codes 1Q84 and 1Q83, respectively)

†To whom correspondence may be addressed. E-mail: marchot.p@jean-roche.univ-mrs.fr or yves@afmb.cnrs-mrs.fr.

BIOCHEMISTRY

Table 1. Data collection and refinement statistics

	TZ2PA6 isomer complexed to mAChE	
	anti1	*syn1*
Data collection*		
Beamline (European Synchrotron Radiation Facility)	ID14-EH1	ID14-EH2
Wavelength, Å	0.933	0.933
Resolution range, Å	25–2.45	25–2.65
Total observations	549,476	513,851
Unique reflections	74,834	59,650
Multiplicity	3.9	3.6
Completeness, %	99.8 (99.7)	99.8 (99.9)
I/σ (I)	9.3 (1.8)	8.2 (1.8)
R_{sym}†	5.7 (43.5)	6.5 (42.0)
Refinement‡		
R factor/R_{free}, %	18.4/21.4	18.1/22.0
rms deviation§		
Bonds, Å/angles, °	0.015/1.5	0.015/1.5
Chiral volume, Å^3	0.085	0.084
Mean *B* factors, Å		
Main/side chains	53.4/55.2	49.7/51.6
Solvent/carbohydrate	50.8/91.5	46.7/95.2
Ligand/polyethylene glycol	63.5/72.2	57.2/66.3
rms deviation on *B* factors, Å^2		
Main/side chains	0.9/1.6	0.9/1.6

*Values in parentheses are those for the last shell.
†$R_{sym} = |I - \langle I\rangle|/\Sigma I$, where I is an individual reflection measurement and $\langle I\rangle$ is the mean intensity for symmetry-related reflections.
‡R factor $= \Sigma||F_o| - |F_c||/\Sigma|F_o|$, where F_o and F_c are observed and calculated structure factors, respectively. R_{free} is calculated for 2% of randomly selected reflections excluded from refinement.
§rms deviation from ideal values.

of reactants causing the higher affinity *syn1* isomer to be the sole reaction product *in situ*, these structures also provide insights on the cycloaddition reaction occurring on a flexible protein template and at a locus remote from the anchoring binding sites of the precursors. Thus, the unique structure of the complex captured by click chemistry leads to an unusual strategy for drug design where the most selective agents induce distinctive conformational states of the target.

Experimental Procedures

Preparation and Analysis of the Complexes. The TZ2PA6 *anti1* and *syn1* isomers were synthesized as described (7). Monomeric mAChE expressed from human embryonic kidney-293 cells (9) was purified by affinity chromatography by using propidium elution (10). The *anti1*- and *syn1*-mAChE complexes were prepared by using a 2-fold molar excess of the inhibitors and concentrations well above their K_ds (≈135 μM i.e., 15 $10^6 \times K_{i(anti)}$ and 330 $10^6 \times K_{i(syn)}$; Table 2) (7, 10). Titration of the isomer stock solutions (ε_{490nm} = 6,000 $M^{-1}\cdot cm^{-1}$) and analysis of the complex solutions were carried out spectrophotometrically (10).

Crystallization and Data Collection. Crystallization was achieved at 4°C by vapor diffusion by using hanging drops (1–2 μl) and a protein-to-well solution ratio of 1:1 with polyethylene glycol-600 25–32% (vol/vol) in 20–100 mM Hepes, pH 6.0–7.5, as the well solution. The crystals were directly flash-cooled in the nitrogen gas stream (100 K); optimal occupancies of the crystalline PASs were controlled by spectrophotometry before data collection (10). The crystals belonged to the orthorhombic space group $P2_12_12_1$ with unit cell dimensions a = 79.7 Å, b = 111.9 Å, and c = 226.5 Å.

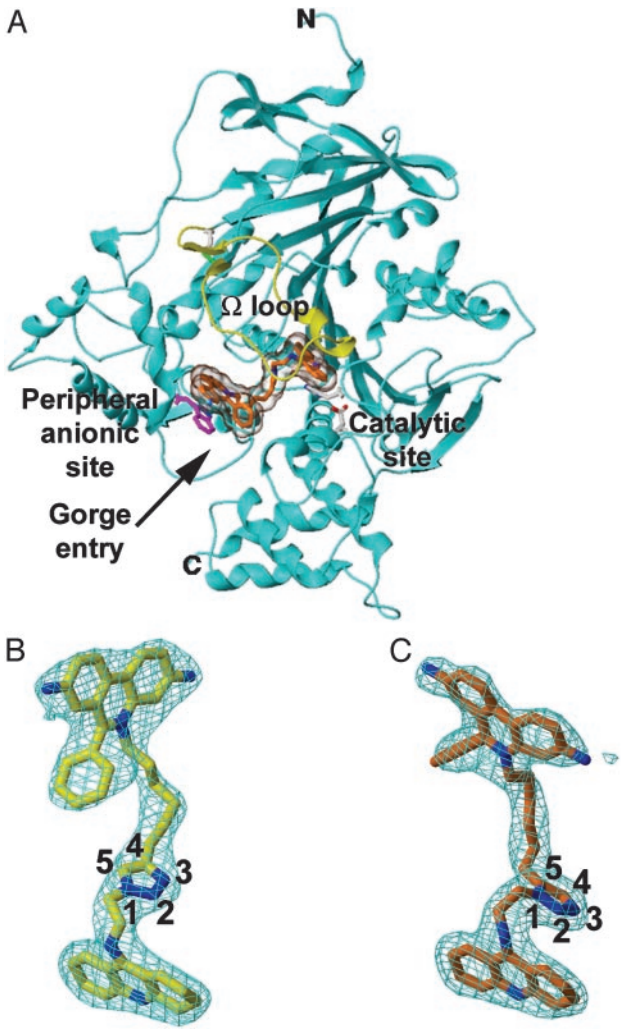

Fig. 1. Overall fold and structural quality of the TZ2PA6–mAChE complexes. (*A*) Overall view of the mAChE molecule (cyan ribbon) showing the *syn1* isomer (orange bonds; transparent molecular surface) bound within the enzyme active-site gorge; the long Ω loop Cys-69-Cys-96 is displayed in yellow. (*B* and *C*) Determined structures of the bound *anti1* and *syn1* isomers (yellow and orange bonds, respectively; blue nitrogens; numbered triazole atoms; same orientation as in Scheme 1), with the respective 2.45- and 2.65-Å resolution final $2F_o-F_c$ electron density maps contoured at 1 σ (cyan).

Oscillation images were integrated with DENZO (12), and data were scaled and merged with SCALA (13).

Structure Determination and Refinement. Coordinates of the *anti1* and *syn1* molecules were obtained from docked simulations of TZ2PA6–TcAChE complexes (7). The apo-mAChE structure (Protein Data Bank ID code 1J06) (10) without solvent was used as a starting model to refine the *anti1*- and *syn1*-mAChE complex structures with CNS (14) and REFMAC (15) (Table 1). Rigid-body refinements on each of the two subunits in the crystalline mAChE dimer (10) gave R factor values of 25.2% and 24.8% (R_{free} values of 25.8% and 25.3%) for the *anti1* and *syn1* complexes, respectively, by using all data in the 25- to 2.45/2.65-Å resolution range. The resulting $2F_o-F_c$ and F_o-F_c electron density maps were used to position the inhibitors and correct the protein model with the graphics program TURBO-FRODO (16).

The final two TZ2PA6–mAChE structures comprise residues Glu-1-Ala-541 and Glu-4-Thr-540 for the two mAChE mole-

Table 2. Kinetic parameters for inhibition of various cholinesterases by the TZ2PA6 isomers

	syn1			*anti1*		
Enzyme	k_{on}, 10^{10} $M^{-1}\cdot min^{-1}$	k_{off}, 10^{-3} min^{-1}	K_i, fM	k_{on}, 10^{10} $M^{-1}\cdot min^{-1}$	k_{off}, 10^{-3} min^{-1}	K_i, fM
mAChE*	1.7	7.1	410	2.5	220	8,900
mAChE mutant Trp286Ala	0.94	19	2,000	0.87	1,800	210,000
AChE, *Electrophorus electricus**	1.5	1.5	99	1.8	250	14,000
AChE, *Torpedo californica**	1.4	1.1	77	3.2	23	720
AChE, *Drosophila melanogaster*	2.0	72	3,600	3.4	58	1,700
Butyrylcholinesterase, mouse	0.36	2.6	720	0.69	3.2	460

Parameters are means of $n \geq 3$ individual values with SD $\leq$ 20%.
*Modified from ref. 7.

cules in the asymmetric unit (10). High-temperature factors and weak electron densities are associated with residues Cys-257, Pro-258, and Asp-265 in the short Ω loop Cys-257-Cys-272 and with the surface loop region Asp-491-Pro-498. The average rms deviation (rmsd) between the *anti1* and *syn1* complex structures is 0.24 Å for 535 Cα atoms. Between the *anti1* and *syn1* complexes and the apo form, the rmsds are 0.19 and 0.23 Å for 534 and 533 Cα atoms, respectively. The stereochemistries of the bound isomers were checked by using the MM2 force field as implemented in MACROMODEL (17). Those of the structures were analyzed with PROCHECK (18); with the exception of the catalytic Ser-203, no residues were found in the disallowed regions of the Ramachandran plot. Figs. 1–3 were generated with SPOCK (19) and RASTER3D (20).

Inhibition Studies. Inhibition constants were measured from the ratio of dissociation and association rates ascertained by conventional mixing and stopped-flow instrumentation (7). The mAChE Trp286Ala mutant was expressed, sequence verified, and concentrated from the expression medium as described (21). Purified AChE from *D. melanogaster* was a gift from D. Fournier (Institut de Pharmacologie et de Biologie Structurale, Toulouse, France).

Results and Discussion

Overall View of the TZ2PA6–mAChE Complexes. The structures of mAChE in complexes with the *anti1* and *syn1* regioisomers (Fig. 1) show the canonical catalytic subunit, made up of a 12-stranded central β-sheet surrounded by 14 α-helices (10, 22, 23), and well-ordered bound inhibitor molecules. The isomer-binding site may be deconstructed into three discrete loci: (*i*) the active center at the base of the gorge that binds the tacrine moiety; (*ii*) an intervening site in the constricted region within the gorge that associates with the triazole moiety and adjacent methylene groups; and (*iii*) the PAS at the rim of the gorge that binds the phenylphenanthridinium moiety.

The *anti1*–mAChE Complex. In the *anti1* complex, the tacrine moiety is positioned at the base of the mAChE gorge similar to the *T. californica* AChE–tacrine complex (11) (Fig. 2*A*). However, the density maps clearly reveal a slight bend in the moiety that may enhance π-π stacking of the tetrahydroaminoacridine ring inserted between the Trp-86 and Tyr-337 aromatic side chains. At the region of constriction formed by the side chains of Tyr-124, Phe-297, Tyr-337, and Phe-338, ≈5–8 Å into the gorge, the triazole establishes van der Waals contacts with the Phe-297 and Tyr-341 side chains. The hydroxyl groups of Tyr-337 and Tyr-124, on opposite sides of the gorge, are hydrogen-bonded to the triazole N2 and N3 atoms and may interact with the heteroaromatic π-system. The dimethylene linker connecting the tacrine and triazole is well ordered within the gorge and in van der Waals contact with the side chains of the conserved residues Asp-74, Tyr-124, and Tyr-341.

At the PAS, the phenylphenanthridinium moiety is positioned by the hexamethylene chain that links it to the triazole. Major interactions include a near-parallel stacking of the planar phenanthridinium with the Trp-286 indole, an edge-to-face arrangement with the Tyr-72 ring, and stabilizing interactions with the Ser-293 hydoxyl and Gln-291 carbonyl (Figs. 2*A* and 3*A*). The *anti1* exocyclic phenyl moiety, nearly buried at the gorge entrance and in a T shaped arrangement with the Tyr-72 and Trp-286 side chains, orients to establish van der Waals contacts with the Asp-74, Tyr-124, and Tyr-341 side chains and hydrogen bonds with the Tyr-72 hydroxyl and Ser-293 N, O, and Oγ atoms. Partial delocalization of electrons between the Trp-286 indole and the phenanthridinium observed in the density maps suggests formation of a charge–transfer complex, similar to that observed in the decidium–mAChE complex (10) (Fig. 2*D*).

The architecture of the PAS region in the *anti1*–mAChE complex (Figs. 2*A* and 3*A*) is virtually identical to that seen in the decidium– and propidium–mAChE complexes (10), and the major interactions involved in the phenanthridinium–Trp-286 stacking are retained (Fig. 2*D*). Yet the phenylphenanthridinium adopts distinctive orientations in the PAS in the three complexes. In the *anti1* complex, the phenanthridinium is rotated by ≈180° around its centroid axis, whereas this centroid is translated by 1.5 Å from its position in the other two complexes. This positioning leads to stabilizing interactions of the *anti1* phenanthridinium with the Gln-291 and Ser-293 side chains, instead of the His-287 imidazole located across the gorge opening, and to a distinct environment for the exocyclic phenyl group. This versatility in the rotational and translational orientations of the bound phenylphenanthridinium relative to the Trp-286 side chain adds a new dimension to the design of molecules that associate with the PAS region.

The *syn1*–mAChE Complex. The structure of the *syn1*–mAChE complex differs considerably from that of the *anti1*–mAChE complex, due to the respective 1,5- and 1,4-disubstitution of the *syn1* and *anti1* 1,2,3-triazole rings (Scheme 1, Fig. 1). The *anti1* isomer adopts an elongated flat shape, whereas the *syn1* isomer presents a corkscrew-like topology that provides greater surface complementarity with the gorge walls, resulting in fewer solvent-filled voids around the bound *syn1* (Figs. 2 *B* and *C* and 3*B*). Whereas the tacrine moiety in both complexes is positioned similarly within the active site, the triazole in the *syn1* complex is shifted 2 Å deeper into the gorge, where it is held in place by the tacrine ring and the Phe-297 and Phe-338 side chains. Consequently, a single π-aromatic interaction may exist between the *syn1* triazole and Tyr-124 hydroxyl, and a water-bridged hydrogen bond is created between the triazole N3 and the catalytic Ser-203 Oγ and Gly-121 amide backbone. Additional van der Waals contacts occur between the triazole and the Gly-121-Gly-122 dipeptide backbone and Tyr-124 side chain. The shifted *syn1* triazole occludes the Tyr-337 ring, which sweeps

BIOCHEMISTRY

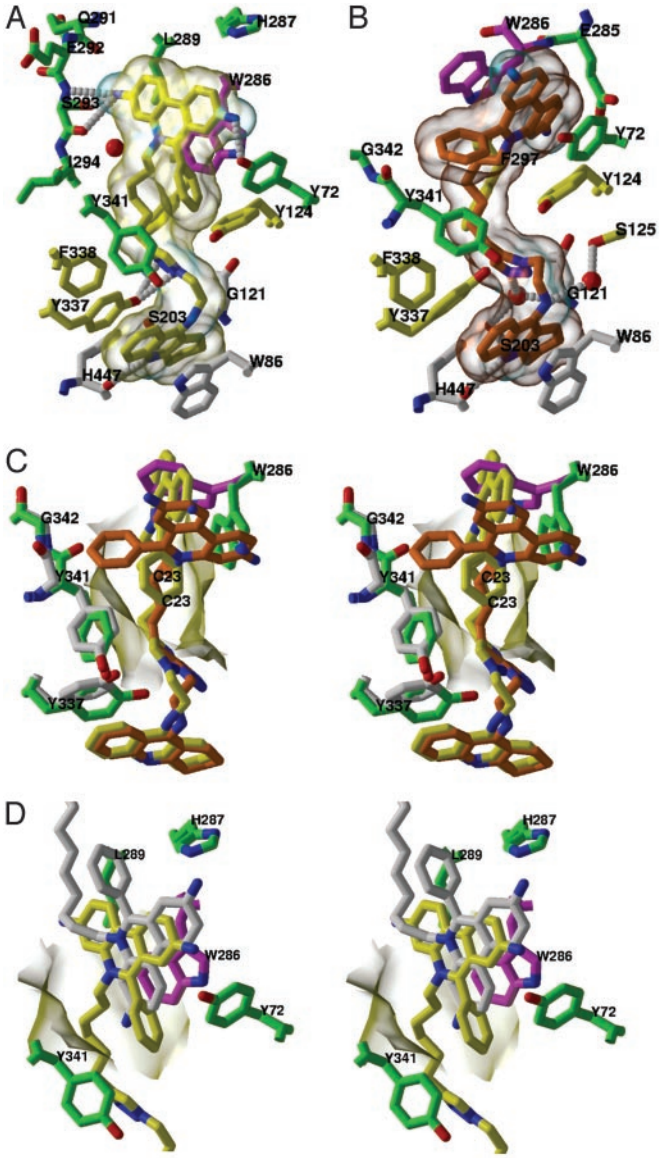

Fig. 2. Close-up views of the TZ2PA6–mAChE complexes. (*A* and *B*) Bound *anti1* and *syn1* isomers (colored as in Fig. 1) with interacting mAChE side chains colored white, yellow, and green/magenta (blue, nitrogens; red, oxygens) for those that respectively interact with the tacrine, triazole, and phenanthridinium moieties of the isomers. The isomer molecular surfaces are displayed in transparency. The side chains of the catalytic residues Ser-203, Glu-334, and His-447 are shown as white bonds, and hydrogen bonds between mAChE residues and the isomers are shown as white dotted lines. (*C*) Stereo superimposition of the *anti1* and *syn1* complexes (colored as in *A* and *B*) according to all Cα atoms of mAChE. The side chains of residues Trp-286 and Tyr-337 and of dipeptide Tyr-341-Gly-342, which adopt distinctive positions in the complexes, are shown in magenta and green, respectively. The χ values for the Trp-286 side chain are (*anti* $\chi_1 = -73°$, $\chi_2 = 100°$; *syn* $\chi_1 = -158°$, $\chi_2 = 50°$). (*D*) Stereo superimposition of the *anti1* complex with the decidium–mAChE complex (Protein Data Bank ID code 1J07; ref. 10) according to all Cα atoms of mAChE in the two complexes. The *anti1* and decidium phenylphenanthridinium moieties (yellow and white bonds, respectively; blue, nitrogens) adopt distinct positions and orientations relative to Trp-286 in the PAS, whereas their alkyl chains diverge. The side chains of the PAS residues are highlighted in green (blue, nitrogens; red, oxygens). The mAChE molecular surface buried at the *anti1* complex interface is displayed in transparency.

out in a 60° arc, resulting in a hydroxyl group displacement of 4.5 Å and in new interactions with the Tyr-341 ring near the gorge entry.

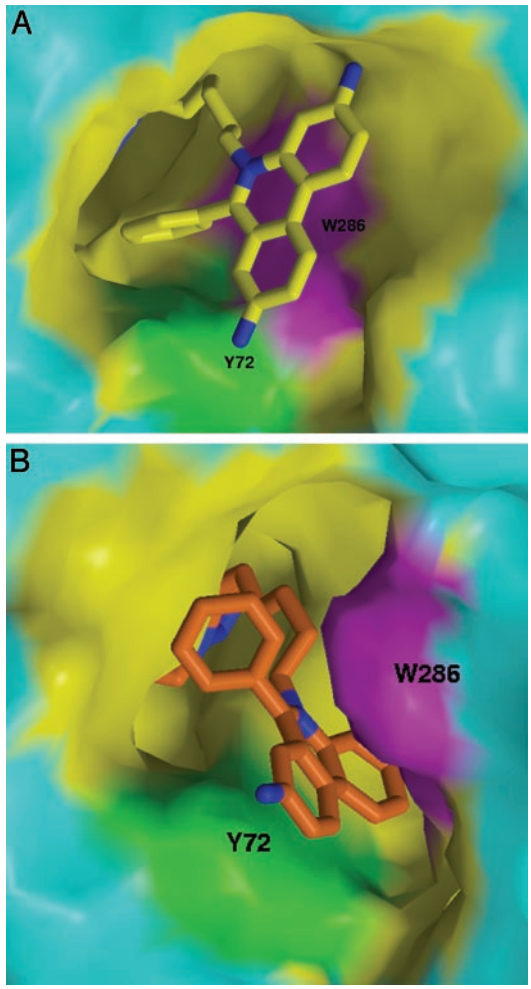

Fig. 3. Distinctive topographies of the PAS regions in the *anti1* and *syn1* complexes. Views of the PAS region of mAChE bound to the phenanthridinium moiety present in the *anti1* (*A*) and *syn1* (*B*) isomers (colored as in Figs. 1 and 2). The mAChE molecular surfaces buried at the complex interfaces are shown in yellow, with the Tyr-72 and Trp-286 side chains highlighted in green and magenta, respectively. The mAChE surface areas (Connolly's surfaces) buried to a 1.6-Å radius probe at the *anti1* and *syn1* complex interfaces by the phenylphenanthridinium and linker first carbon are 256 and 313 Å^2 (the double-face burying of the *syn1* phenanthridinium being counterbalanced by the deeper burying of the *anti1* phenyl). The gorge mouth openings (Richards' surface) for the *anti1* and *syn1* complexes are 14 and 29 Å^2, respectively.

The position and orientation of the *syn1* triazole at the gorge constriction influence the phenylphenanthridinium position at the PAS (Figs. 2 *B* and *C* and 3*B*). Compared to the *anti1* complex, the overall span of the linker is shortened by 1.5 Å in the more compact *syn1* triazole, a value close to the length of a C–C bond (Fig. 1 *B* and *C*). As a result of the reduced linking distance, the *syn1* phenanthridinium moiety is constrained to a narrow region deep within the gorge where it would sterically clash with the Trp-286 indole. This causes the Trp-286 side chain to be dislodged from the PAS surface and to swing into the solvent, with differences of 85° and 50° in the χ_1 and χ_2 values, respectively. This distinct side chain conformation enlarges the opening at the gorge rim 2-fold, creating a 10 × 9 Å groove delimited by the Tyr-72 and uniquely positioned Trp-286 side chains on each side and by Glu-285 at its base, wherein the phenanthridinium tightly intercalates (Figs. 2 *B* and *C* and 3*B*). Hence, the aromatic plate of the *syn1* phenanthridinium, oriented 90° from its position in the *anti1* complex, is wedged

neatly between the two aromatic side chains where it is stabilized by π-π interactions with centroids separated by 3.6–3.8 Å. This causes the phenyl group to become solvent exposed and establish discrete van der Waals contacts with residues Leu-76, Tyr-341, and Gly-342 at the gorge rim.

Kinetic Analysis of *syn1* and *anti1* Isomer Binding. Comparison of the relative rates of association and dissociation shows that the enhanced affinity of the *syn1* isomer for mAChE largely results from a slower dissociation rate (Table 2). The small differences seen in the association rates would be anticipated in view of the rates being at or near the diffusion rate limit. Hence the enhanced affinity of the *syn1* isomer is reflected in a greater activation barrier for dissociation of the complex. Several conformational changes and positional rearrangements of side chains observed within the PAS and active-site gorge correlate with the *syn1* isomer being more tightly sequestered in the active site gorge.

The *syn1* isomer displays up to 5-fold greater affinity for *E. electricus* and *T. californica* AChEs than for mAChE, and the selectivity of *E. electricus* AChE for the *syn1* isomer is as much as 300-fold higher than that of any other AChE species assayed (Table 2). Only low-resolution structures of *E. electricus* AChE are available (24), but the limited sequence differences found at the PAS and within the gorge do not reveal particular determinants responsible for the higher selectivity. In contrast, *D. melanogaster* AChE, with its Glu, Tyr, and Met substitutions for mAChE residues Tyr-72, Asp-74, and Tyr-124, and mouse butyrylcholinesterase, with its Arg and Asn substitutions for Trp-286 and Tyr-72 (see http://bioweb.ensam.inra.fr/ESTHER/general?what = index), show an inverted but small selectivity for the *anti1* isomer, consistent with a more open gorge and fewer aromatic side chains at the PAS in these enzymes. Moreover, removal of the indole ring at the rim of the mAChE gorge by a Trp286Ala mutation results in higher dissociation rates and up to 20-fold reduction in affinity for the *syn1* and *anti1* complexes. These results further emphasize the importance of the peripheral aromatic side chains in trapping the *syn1* phenanthridinium and of Trp-286 in stabilizing both complexes despite the distinctive orientations of the indole side chain.

Functional Role of the Central Triazole Moiety. The triazole moieties of the *syn1*- and *anti1*-mAChE complexes are both tightly bound within the gorge, due to rearrangements in both ligand position and mAChE conformation (Fig. 2). Hence, the triazoles actively contribute to the binding interactions in the respective complexes instead of acting as passive linkers. The high affinities of the complexes (Table 2) arise not only from proximity reducing entropic contributions for a "divalent" ligand with separate binding groups but also from interactions along the gorge wall. The observation that the alternate synthesis product TZ6PA2 with inverted dimethylene and hexamethylene linkers is a weak AChE inhibitor (7) provides additional evidence for specific position-sensitive triazole contributions to the overall binding energy. The formative adaptability of this five-membered heterocycle is reflected in *syn1* cycloaddition occurring with the azide and acetylene extended in a parallel orientation, effectively shortening the intervening linker through the triazole by one bond length, whereas they would lie antiparallel in formation of the *anti1* triazole product (7). The triazole's large dipole (>5 Debye), which bisects the ring plane near atoms N3 and C5 (Scheme 1, Fig. 1 *B* and *C*), and the capacity of the N2 and N3 electron lone pairs to serve as hydrogen bond acceptors not only enhance binding affinity but also contribute to the efficiency of the 1,3-dipolar-coupling reaction. The conformation of the *syn1* complex is congruent with *syn1*'s shorter linker, compared to the *anti1* complex. This is evident from the positioning of the phenanthridinium at the PAS, where it resides closer to the tetrahydroaminoacridine in the *syn1* than in the *anti1* complex (Fig. 1 *B* and *C*, Fig. 2*C*). To achieve this disposition of proximal reactants, a substantial conformational change occurs at the rim of the gorge with a secondary change evident in the vicinity of the triazole formed by the cycloaddition (Figs. 2*C* and 3). Hence, the reactivity of the azide and acetylene precursors in the gorge and the resulting affinity of the triazole formed could not have been predicted from structures of apo-AChE (10) or of complexes with close congeners to the precursors (10, 11). To date, inhibitors containing substituted 1,2,3-triazoles have been observed only in plant glycolate oxidase inhibitors (25) and β-lactam antimicrobials (26).

Functional Role of the Trp-286 Indole. Most AChE crystal structures show the Trp-286 side chain centered in the PAS with one face of the indole buried at the rim of the gorge and the other occluded by either a symmetry-related AChE molecule or a bound PAS ligand (ref. 3, and subsequent structures derived from the same TcAChE crystal form; refs. 10, 11, 22, 23, 27, and 28). Only the apo-mAChE structure (10), solved from the crystal form used here, shows the Trp-286 external face fully accessible to solvent, providing it with potential mobility. Indeed, binding of the *syn1* isomer displaces the Trp-286 side chain from the AChE hydrophobic core toward the solvent, with one face of the indole now stacked with the phenanthridinium and the other face still exposed to the solvent and in van der Waals contact with Leu-289 (Figs. 2*C* and 3). One of the phenanthridinium rings is buried in a near-parallel stacking interaction with the Tyr-124 ring at the bottom of the groove, whereas the other two rings insert into the Trp-286-Tyr-72 parallel sandwich. The buried phenanthridinium amino group is hydrogen bonded to Glu-285. Whereas the phenanthridinium ring system in the bound *anti1* isomer is virtually planar, the *syn1* system adopts a slightly curved shape conforming to the induced groove where it intercalates.

Indirect evidence suggests that the PAS region, with its surface-exposed aromatic groups, may be responsible for the adhesion properties of AChE (29). Recognition and adhesion play important roles in synapse maintenance, as seen with the structurally related neuroligins (30). They may also play a role for the AChE-promoted nucleation of amyloid peptides in the Alzheimer's disease pathogenesis (31). The flip in the Trp-286 indole and the newfound π-π and cation–π interactions seen in the *syn* complex raise the possibility that an open conformation of AChE with distinctive exposure of aromatic groups is involved in these adhesion functions. π-orbital stacking mediated by aromatic side chains is instrumental in other molecular recognition and cell adhesion processes (32). Other intercalations of polycylic aromatic compounds between protein aromatic side chains or nucleotide bases involve the isoalloxazine moiety of the flavin cofactor and flavodoxin (33); ethidium derivatives and the multidrug-resistant-binding protein QacR (34) and adjacent base pairs (see Nucleic Acid Database, code 1JTY); the benzothiazole moiety of thioflavin and DNA (35) and β-sheet amyloid structures (36); and perhaps thioflavin and the PAS of AChE (37).

Role of the AChE Gorge Flexibility in Catalysis and Inhibitor Binding. Controversy surrounds how AChE, with its catalytic triad at the base of a narrow gorge, sustains high catalytic efficiency. Alternate portals for substrate and product access have been proposed (38); however, catalytic and inhibitor-binding parameters are influenced only by mutations in the gorge (21) and not in the vicinity of the putative additional portals (39). Rapid fluctuations giving rise to transient enlargements of the gorge appear critical (40). Ligand binding evidently induces a closed gorge state, whereas the unliganded enzyme seems to fluctuate rapidly between multiple states with varying degrees of gorge openness (41, 42).

Previous structural analysis of PAS ligands associated with

mAChE showed that the tips of the long Ω loop Cys-69-Cys-96 and loop Val-340-Gly-342 bordering on the gorge (Fig. 1*A*) possessed sufficient mobility to enlarge the gorge entry, thereby facilitating access to and from the active center (10). In fact, only the *syn1*–mAChE complex exhibits an increase of up to 12 Å in the mean temperature factors for residues at the loop tips where movement of 1.2 Å of Leu-76 and an inversion of the Gly-342 carbonyl carbon occur; the weak electron densities for the Leu-76 and Tyr-341 side chains are also consistent with substantial localized fluctuations. Hence, the flexibility of the AChE long Ω loop differs from the hinge-like motion of a homologous loop that, in the structurally related lipases, forms a rigid flap and opens only in the presence of the lipid substrate (43, 44). Moreover, ligand binding to AChE may cause the gorge to collapse around the ligand, minimizing internal dimensions (41, 42). This notion is supported by the observed repositioning of the Tyr-337 side chain and associated perturbation of Tyr-341, which not only alter the gorge shape but also enlarge its width at the position of constriction to accommodate the *syn1* triazole (Fig. 2*C*). Such large conformational changes involving these residues were not observed for the PAS or active center complexes from which the precursor reactants were designed (10, 11). These computational and experimental results point to concerted fluctuations all along the gorge, which may facilitate access of incoming substrate to the active site at the gorge base and presumably occur in short time frames relative to diffusional translation of substrate (40).

In summary, the use of the enzyme active-site gorge as an atomic-scale template for inhibitor synthesis (7) and of structural analyses of the *anti1*- and *syn1*-mAChE complexes has revealed (*i*) an *in situ* phemonenon (7) that bears an uncanny resemblance to pioneering studies begun in 1983 by W. L. Mock (45); (*ii*) inherent flexibility and conformational fluctuations in the AChE molecule; and (*iii*) a most stable and selective complex that could not have been predicted from the apo-enzyme structure (10). The highly exergonic nature of the 1,3-dipolar-[2 + 3]-cycloaddition ($\Delta H > 50$ kcal/mol) has allowed us to immobilize and then identify by structural means an otherwise minor abundance conformation of the enzyme. Because only the higher-affinity *syn1*-triazole regioisomer is associated with major changes in enzyme conformation, the crystalline *syn1*–mAChE complex becomes the lead template in the design of selective pharmacologic agents directed toward the catalytic or noncatalytic functions of AChE. If, in fact, AChE through its PAS plays a role in synaptic adhesion processes and in nucleating plaque formation associated with dementia (29), then AChE inhibitors that also influence surface conformation may offer a means of enhancing therapeutic efficacy.

We are grateful to D. Fournier for providing the *D. melanogaster* enzyme, L. Green for synthesis of the regioisomers; F. Grynszpan, M. G. Finn, and W. G. Lewis for discussion; M. Juin for assistance in crystallogenesis; and G. Sulzenbacher, M. Czjzek, and the ID14 staff of the European Synchrotron Radiation Facility for expert assistance in data collection. This work was supported by grants from the Association Française contre les Myopathies (to P.M.); U.S. Public Health Service (R37-GM18360) and Department of Army Medical Defense (17-1-8014) (to P.T.); and National Institutes of Health (GM 28384), National Science Foundation (CHE-9985553), National Institute of General Medical Sciences, and the W. M. Keck Foundation (to K.B.S.).

1. Argyl-Robertson, D. (1863) *Edinb. Med. J.* **8,** 815–820.
2. Dale, H. H. (1914) *J. Pharmacol. Exp. Ther.* **6,** 147–190.
3. Sussman, J. L., Harel, M., Frolow, F., Oefner, C., Goldman, A., Toker, L. & Silman, I. (1991) *Science* **253,** 872–879.
4. Changeux, J.-P. (1966) *Mol. Pharmacol.* **2,** 369–392.
5. Taylor, P. & Lappi, S. (1975) *Biochemistry* **14,** 1989–1997.
6. Taylor, P. (2001) in *Goodman and Gilman's Pharmacological Basis of Therapeutics* (eds. Hardman, J. G. & Limbird, L. E.), 10th Ed., pp. 175–192.
7. Lewis, W. G., Green, L. G., Grynszpan, F., Radić, Z., Carlier, P. R., Taylor, P., Finn, M. G. & Sharpless, K. B. (2002) *Angew. Chem. Int. Ed.* **41,** 1053–1057.
8. Rachinsky, T. L., Camp, S., Li, Y., Ekström, J., Newton, M. & Taylor, P. (1990) *Neuron* **5,** 317–327.
9. Marchot, P., Ravelli, R. B. G., Raves, M. L., Bourne, Y., Vellom, D. C., Kanter, J., Camp, S., Sussman, J. L. & Taylor, P. (1996) *Protein Sci.* **5,** 672–679.
10. Bourne, Y., Taylor, P., Radić, Z. & Marchot, P. (2003) *EMBO J.* **22,** 1–12.
11. Harel, M., Schalk, I., Ehret-Sabatier, L., Bouet, F., Goeldner, M., Hirth, C., Axelsen, P. H., Silman, I. & Sussman, J. L. (1993) *Proc. Natl. Acad. Sci. USA* **90,** 9031–9035.
12. Otwinowski, Z. & Minor, W. (1997) *Methods Enzymol.* **276,** 307–326.
13. Collaborative Computational Project Number 4 (1994) *Acta Crystallogr. D* **50,** 760–763.
14. Brünger, A. T., Adams, P. D., Marius Clore, G., DeLano, W. L., Gros, P., Grosse-Kunstleve, R. W., Jiang, J.-S., Kuszewski, J., Nilges, M., Pannu, N. S., *et al.* (1998) *Acta Crystallogr. D* **54,** 905–909.
15. Murshudov, G., Vagin, A. & Dodson, E. J. (1997) *Acta Crystallogr. D* **53,** 240–255.
16. Roussel, A. & Cambillau, C. (1989) in *Silicon Graphics Geometry Partners Directory*, eds. Silicon Graphics Committee (Silicon Graphics, Mountain View, CA) , pp. 77–78.
17. Mohamadi, F., Richards, N. G. J., Guida, W. C., Liskamp, R., Lipton, M., Caufield, C., Chang, G., Hendrickson, T. & Still, W. C. (1990) *J. Comput. Chem.* **11,** 440–467.
18. Laskowski, R. A., MacArthur, M. W., Moss, D. S. & Thornton, J. M. (1993) *J. Appl. Crystallogr.* **26,** 283–291.
19. Christopher, J. A. (1998) SPOCK (Center for Macromolecular Design, Texas A&M University, College Station, TX).
20. Merritt, E. A. & Bacon, D. J. (1997) *Methods Enzymol.* **277,** 505–524.
21. Radić, Z., Pickering, N. A., Vellom, D. C., Camp, S. & Taylor, P. (1993) *Biochemistry* **32,** 12074–12084.
22. Bourne, Y., Taylor, P. & Marchot, P. (1995) *Cell* **83,** 503–512.
23. Bourne, Y., Taylor, P., Bougis, P. E. & Marchot, P. (1999) *J. Biol. Chem.* **274,** 2963–2970.
24. Bourne, Y., Grassi, J., Bougis, P. E. & Marchot, P. (1999) *J. Biol. Chem.* **274,** 30370–30376.
25. Stenberg, K. & Lindqvist, Y. (1997) *Protein Sci.* **6,** 1009–1015.
26. Kuzin, A. P., Nukaga, M., Nukaga, Y., Hujer, A. M., Bonomo, R. A. & Knox, J. R. (2001) *Biochemistry* **40,** 1861–1866.
27. Harel, M., Kleywegt, G. J., Ravelli, R. B., Silman, I. & Sussman, J. L. (1995) *Structure (London)* **3,** 1355–1366.
28. Kryger, G., Silman, I. & Sussman, J. L. (1999) *Acta Crystallogr. D* **56,** 1385–1394.
29. Soreq, H. & Seidman, S. (2001) *Nat. Rev. Neurosci.* **2,** 294–302.
30. Ichtchenko, K., Nguyen, T. & Sudhof, T. C. (1996) *J. Biol. Chem.* **271,** 2676–2682.
31. Inestrosa, N. C., Alvarez, A., Perez, C. A., Moreno, R. D., Vicente, M., Linker, C., Casanueva, O. I., Soto, C. & Garrido, J. (1996) *Neuron* **16,** 881–891.
32. Zacharias, N. & Dougherty, D. A. (2002) *Trends Pharmacol. Sci.* **23,** 281–287.
33. Genzor, C. G., Perales-Alcon, A., Sancho, J. & Romero, A. (1996) *Nat. Struct. Biol.* **3,** 329–332.
34. Schumacher, M. A., Miller, M. C., Grkovic, S., Brown, M. H., Skurray, R. A. & Brennan, R. G. (2001) *Science* **294,** 2158–2163.
35. Canete, M., Villanueva, A., Juarranz, A. & Stockert, J. C. (1987) *Cell. Mol. Biol.* **33,** 191–199.
36. LeVine, H., III (1999) *Methods Enzymol.* **309,** 274–284.
37. De Ferrari, G. V., Mallender, W. D., Inestrosa, N. C. & Rosenberry, T. L. (2001) *J. Biol. Chem.* **276,** 23282–23287.
38. Gilson, M. K., Straatsma, T. P., McCammon, J. A., Ripoll, D. R., Faerman, C. H., Axelsen, P. H., Silman, I. & Sussman, J. L. (1994) *Science* **263,** 1276–1278.
39. Kronman, C., Ordentlich, A., Barak, D., Velan, B. & Shafferman, A. (1994) *J. Biol. Chem.* **269,** 27819–27822.
40. Shen, T., Tai, K., Henchman, R. H. & McCammon, J. A. (2002) *Acc. Chem. Res.* **35,** 332–340.
41. Shi, J., Radić, Z. & Taylor, P. (2002) *J. Biol. Chem.* **277,** 43301–43308.
42. Shi, J., Tai, K., McCammon, A. J., Taylor, P. & Johnson, D. A. (2003) *J. Biol. Chem.* **278,** 30905–30911.
43. Cygler, M., Schrag, J., Sussman, J. L., Harel, M., Silman, I., Gentry, M. K. & Doctor, B. P. (1993) *Protein Sci.* **2,** 366–382.
44. Grochulski, P., Li, Y., Schrag, J. D. & Cygler, M. (1994) *Protein Sci.* **3,** 82–91.
45. Mock, W.L. (1995) *Top. Curr. Chem.* **175,** 1–24.